JOURNAL OF CATALYSIS 153, 144–157 (1995)

Fe Promoted Rh-Clusters in Zeolite NaY: Characterization and Catalytic Performance in CO Hydrogenation

V. Schünemann,* H. Treviño,* G. D. Lei,* D. C. Tomczak,* W. M. H. Sachtler,*,[1] K. Fogash,† and J. A. Dumesic†

*V. N. Ipatieff Laboratory, Center for Catalysis and Surface Science, Department of Chemistry, Northwestern University, Evanston, Illinois 60208; and †Department of Chemical Engineering, University of Wisconsin, Madison, Wisconsin 53706

Mössbauer spectroscopy, temperature programmed reduction (TPR), and FTIR of adsorbed CO show that ion exchange of $[Rh(NH_3)_4Cl]Cl_2$ and $FeSO_4$ into NaY, followed by calcination and reduction in H_2 up to 500°C, leads to Fe^{2+} ions and bimetallic RhFe clusters with low Fe^0 content. The selectivity of such catalysts toward oxygenate formation in CO hydrogenation at p = 10 bar, T = 250°C, and H_2/CO = 2 is very low. Much higher oxygenate selectivity, in particular ethanol formation, is observed if Fe^{2+} ions are first hydrolyzed to a hydroxide gel which is subsequently dehydrated. The resulting catalysts contain bimetallic particles of higher Fe^0 content after reduction, coexisting with an Fe^{2+} oxide phase. Transmission electron microscopy shows that a fraction of the metal migrates to the external surface of the NaY support during CO hydrogenation. The results show that Fe exerts two catalytic promoter functions on Rh/NaY catalysts: Fe^0 alloyed with Rh^0 increases the catalytic *activity*; Fe^{2+}, when present as a separate oxide phase in close contact with Rh particles, increases the *selectivity* toward C_{2+} oxygenates. © 1995 Academic Press, Inc.

1. INTRODUCTION

Supported bimetallic catalysts consisting of iron and a platinum group metal (Pt, Rh, Ru, Pd, or Ir) have been studied extensively (1–11). In these systems, the catalytic properties of the platinum group metal are significantly altered by the addition of iron. The conversion of synthesis gas ($CO + H_2$) over Fe, Co, or Ni catalysts has been studied since 1902; it is well known that the product spectrum as well as the activity of the Fe catalysts can be affected by certain promoters. Unpromoted rhodium catalyzes the hydrogenation of CO exclusively towards methane and higher hydrocarbons; the addition of oxidic promoters, such as oxides of Fe, Mn, Zr, V, and La, drastically changes this selectivity in favor of oxygenates, especially ethanol (13–18).

The mode of action of the metal-promoter for rhodium based catalyst systems is still unclear. Niemantsverdriet *et al.* studied SiO_2 supported RhFe; they interpret their Mössbauer spectra by assuming that an irreducible Fe^{3+} phase survives even under reducing conditions (4, 5). Ichikawa *et al.* have elaborated on this concept; they propose a model of catalyst promotion based on a chemical interaction of Rh^0 clusters with Fe^{3+} ions (14, 19). This model is reminiscent of so-called strong metal-support interaction (SMSI), where metallic particles are partly covered by Ti^{3+} or Mn^{2+} ions; however, the SMSI model does not postulate that transition metal ions should persist in a high oxidation state under reducing conditions (20–22).

In a separate paper, we presented experimental evidence that the Mössbauer spectra of Rh–Fe catalysts can be interpreted without postulating that Fe^{3+} should persist under reducing conditions (23). This work showed that Fe^0 in the surface of $RhFe_x$ clusters gives a Mössbauer signal, that happens to be similar to that of Fe^{3+}. As a consequence, an alternative interpretations of the promoter effect of Fe on Rh is proposed. For the related Pd–Fe system, we recently showed that part of the Fe is reduced to Fe^0 and forms an alloy with Pd; no Fe^{3+} is detected under reducing conditions (9). These results are in agreement with those of Guczi *et al.* who observed $PdFe_x$ particles in zeolite X and showed that such bimetallic catalysts lead to an enhanced selectivity of CO hydrogenation towards methanol (24, 25). More recently, we studied the promotion of Rh/NaY with Mn for CO hydrogenation and found that the presence of Mn oxide particles adjacent to Rh clusters is a necessary condition for the formation of oxygenates (16). This work also showed the advantages of using zeolite supports, which offer a unique opportunity to identify the nature of catalyst metal and promoter.

The present work on the RhFe/NaY system continues on this strategy of incorporating catalytic metal and promoter in a zeolite support. The decisive difference between Rh–Fe and Rh–Mn is that under the conditions of syngas catalysis Fe might be reduced to Fe^0 and form an alloy with Rh as it does with Pd, whereas with Rh–Mn it is certain that no Mn^0 is formed under the conditions

[1] To whom correspondence should be addressed.

0021-9517/95 $6.00
Copyright © 1995 by Academic Press, Inc.
All rights of reproduction in any form reserved.

of syngas catalysis. Comparison of the catalytic propensities of Rh–Fe and Rh–Mn should thus provide an opportunity to discern between two potential promoting effects, viz., alloy formation and metal–metal oxide interaction.

In the present work, NaY supported Rh–Fe catalysts have been prepared and tested under standard catalytic conditions at elevated pressure of CO + H_2, both in the presence and in the absence of significant concentrations of acid protons in the zeolite. The chemical states of Fe and Rh were identified by Mössbauer spectroscopy, CO-FTIR and ferromagnetic resonance spectroscopies, temperature programmed reduction (TPR) and transmission electron microscopy.

2. EXPERIMENTAL

2.1. Catalyst Preparation

All samples were prepared by ion-exchange at pH = 4.5–5 of NaY (Linde, LZY-52) with $FeSO_4$ and $[Rh(NH_3)_5Cl]Cl_2$ under a nitrogen atmosphere. The sample compositions were analyzed by ICP. With RhFe/NaY, iron was exchanged first as described by Xu *et al.* (9); subsequent exchange of rhodium was performed by dropwise addition of a solution of $[Rh(NH_3)_5Cl]Cl_2$ in doubly deionized water to the slurry of the previously-iron exchanged Fe/NaY at 80°C under N_2 over a period of 4 days. This exchange was followed by washing with water until the obtained solution was chlorine free. Under these conditions ligand exchange transforms $[Rh(NH_3)_5Cl]^{2+}$ ions to $[Rh(NH_3)_5(H_2O)]^{3+}$ ions (26). The sample then was calcined in an oxygen flow (2000 ml/g–min) up to 500°C with a ramp of 0.5°C/min, followed by calcination at this temperature for 2 h. The flow was switched to Ar for 20 min, and the catalyst was cooled in flowing Ar. ICP elemental analysis showed a metal loading of 2.9 wt% Rh and 1.94 wt% Fe which corresponds to an atomic ratio of Rh/Fe = 0.81 and to 1.5 metal atoms per unit cell.

In some samples, denoted as $RhFe/NaY_{neutr}$, monometallic Rh/NaY was calcined in O_2 up to 500°C and treated up to 500°C (ramp 8°C/min) with 5% H_2/Ar at a flow of 30 ml/min. This treatment was followed by a second ion exchange, in which the protons that are formed during reduction of the Rh^{3+} to Rh^0, were replaced by Fe^{2+} ions from an aqueous $FeSO_4$ solution. After slurrying overnight under N_2 atmosphere and calcination up to 500°C, the metal loading was 3.0 wt% Rh and 2.4 wt% Fe which corresponds to an atomic ratio of Rh/Fe = 0.716.

A third group of samples, designated as $RhFe/NaY_{NaOH}$, was prepared by starting from reduced RhFe/NaY and slurrying the sample overnight in an aqueous NaOH solution at pH = 11, followed by a second calcination up to 500°C. The metal loading corresponded to that of RhFe/NaY (2.9 wt% Rh; 1.9 wt% Fe). Monometallic samples, Rh/NaY and Fe/NaY, were prepared in the same manner as RhFe/NaY, but omitting the addition of the second metal. The metal loadings were 3.1 wt% Rh and 3 wt% Fe. Rh/NaY_{neutr} was stirred overnight, after reduction at 500°C, in an aqueous solution at pH = 4.5–5 under N_2, to simulate the condition of Rh during the preparation of $RhFe/NaY_{neutr}$. After washing, the sample was calcined a second time up to 500°C. Likewise, the samples Rh/NaY_{NaOH} and Fe/NaY_{NaOH} were prepared in the same way as $RhFe/NaY_{NaOH}$, i.e., by immersing the reduced samples in an aqueous NaOH solution at pH = 11 followed by a second calcination.

2.2. Temperature Programmed Reduction

After ion exchange and calcination, the samples were reduced in 5% H_2/Ar by temperature programmed reduction (TPR) as described previously (27). The heating rate during TPR was 8°C/min and the gas flow was 30 ml/min. The temperature program was stopped at 500°C. Following a TPR run, the sample was cooled in H_2/Ar and the flow was switched to Ar (30 ml/min) at room temperature. The hydrogen consumption was obtained by integrating the TPR profiles versus time. The experimental error in the hydrogen consumption is ±5%.

2.3. FMR

Ferromagnetic resonance measurements were carried out on a modified Varian E-4 X-band EPR spectrometer employing 100 kHz field modulation. The observed signals were recorded as the first derivative of the absorption signal with a low microwave power (0.2 mW). The reactor was connected to a small quartz EPR tube. After pretreatment, the reactor was evacuated, and the quartz tube was sealed off without exposure to air. A Varian heating system was used to obtain temperature dependent spectra.

2.4. Mössbauer Spectroscopy

Mössbauer spectra were collected using an Austin Science Associates Model S-600 Mössbauer spectrometer, connected to an IBM compatible PC with a PCAII data collection board. The spectrometer was operated in the constant acceleration mode, with a 50-mCi single line gamma-ray source of ^{57}Co in a Pd matrix. Detection of the gamma rays was achieved with a Kr–CO_2 proportional counter. Isomer shifts are reported relative to α-Fe at room temperature. All samples were calcined to 500°C and then reduced in an *in situ* glass cell with thinned pyrex windows in a flow of dry H_2 up to 500°C with a ramp of 8 K/min. The samples were not exposed to air during the collection of the Mössbauer spectra; the presence of water ligands coordinated to Fe ions can thus be excluded.

It should be noted that the same Mössbauer spectrum was obtained of a sample following reduction in the *in situ* cell with spectral collection in static hydrogen, as

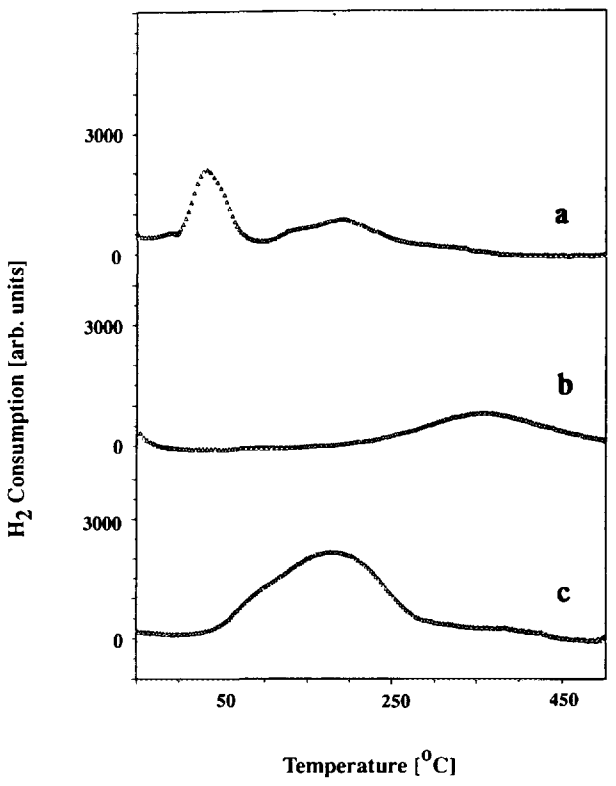

FIG. 1. TPR of Rh/NaY (a), Fe/NaY (b), and RhFe/NaY (c) after calcination up to 500°C.

the Mössbauer spectrum for a sample sealed in a glass ampoule following initial reduction. Thus, contamination of reduced samples during collection of Mössbauer spectra is negligible.

2.5. *FTIR*

Thin self-supporting wafers (8–10 mg/cm^2) of the samples were studied in a quartz cell. All gases (H_2, O_2, Ar, and CO) were UHP-grade. Before use, these gases were passed through traps to remove water and/or oxygen. An additional trap filled with γ-Al_2O_3 in the CO line removes metal carbonyls possibly formed in the gas storage tank. All samples were calcined up to 500°C following by reduction in H_2 up to 500°C. After reduction all samples were cooled in H_2 to room temperature and then treated in flowing He (30 ml/min). A flow of Co (30 ml/min) was passed over the samples at room temperature for 10 min. After subsequent purging with He IR spectra were recorded by a Nicolet 60SX single-beam FTIR spectrometer with a resolution of 1 cm^{-1}.

2.6. *CO-Hydrogenation*

Catalyst samples were tested at 1 MPa and 250°C in a stainless steel flow reactor (XYTEL) with automatic control of the reaction conditions. The H_2/CO ratio was 2 in all cases. The catalytic runs were performed at conversions of typically 5%. Product analysis was done using an HP 5890 gas chromatograph with a 50-m crosslinked methyl silicone capillary column and an FID detector. The number of adsorption sites for the calculation of the turnover frequencies (TOF: number of CO molecules converted per site and second) was determined from the hydrogen adsorption obtained by temperature programmed desorption (TPD) (see Table 2, where the hydrogen adsorption capacity per Rh is given).

2.7. *Transmission Electron Microscopy (TEM)*

After reduction the samples were exposed to air, dispersed on a holy carbon film mounted on an electronmicroscopy grid and transferred immediately to the Hitachi H-2000 transmission electron microscope of the ARAEM facility, Materials Science and Engineering Department, Northwestern University. The same procedure was applied to samples after catalytic tests. The acceleration voltage was 200kV. The samples were scanned with the help of a video camera by using the minimum electron beam intensity to prevent destruction of the zeolite lattice.

3. RESULTS

3.1. *TPR*

The TPR profile of the monometallic Rh/NaY after calcination to 500°C is shown in Fig. 1a. Besides the most prominent hydrogen consumption peak centered at 40°C a broad peak around 200°C with a shoulder at 150°C is observed. On the basis of previous work we assign the dominant peak around 40°C to the reduction of Rh_2O_3 particles; the peaks at 150 and 200°C can be assigned to Rh^{3+} cations located in the super- and the sodalite cages of the NaY support (28, 29). The amount of hydrogen consumed per rhodium atom is given in Table 1. The value of H/Rh = 2.7 rather than 3.0 indicates that some

TABLE 1

Hydrogen Consumption per Metal Atom Obtained from the Integration of the TPR Profiles Presented in Figs. 1–3

RhFe/NaY	Rh/NaY	Fe/NaY
(Rh/Fe) = 0.810 H/(Rh + Fe) = 1.93	H/Rh = 2.7	H/Fe = 0.93
$RhFe_{neutr}$ (Rh/Fe = 0.716) H/(Rh + Fe) = 2.21	Rh/NaY_{neutr} H/Rh = 3.10	Fe/NaY H/Fe = 0.93
$RhFe/NaY_{NaOH}$ (Rh/Fe = 0.81) H/(Rh + Fe) = 2.71	Rh/NaY_{NaOH} H/Rh = 3.50	Fe/NaY_{NaOH} H/Fe = 0.88

Note. Rh/Fe represents the atomic ratios of the metals.

autoreduction took place by the decomposing ammine ligands during calcination, as was shown elsewhere (24, 30); the Rh is completely reduced to the metallic state. The reduction profile of the monometallic Fe/NaY is shown in Fig. 1b. A reduction peak at 350°C is due to the reduction of Fe^{3+} to Fe^{2+} ions (9), which is confirmed by the ratio of H/Fe = 0.93 (Table 1). This result is expected since further reduction of Fe^{2+} ions in NaY is not possible at 500°C (31). The TPR-spectrum of the RhFe/NaY (Fig. 1c) shows a broad peak near 150°C, indicating a shift of the rhodium reduction to higher temperatures and of the iron reduction peak to lower temperatures. The overall hydrogen consumption is H/(Rh + Fe) = 1.93. For a first estimate of the extent of the iron reduction it can be assumed that all rhodium was present as Rh^{3+} after calcination and has been reduced to the metallic state. One then obtains from the atomic ratio of Rh/Fe = 0.81 (Table 1) a hydrogen consumption assigned to iron reduction of H/Fe = 1.06. This ratio indicates that the hydrogen consumption may be slightly larger than required for the reduction of Fe^{3+} to Fe^{2+}, suggesting that 3% of the iron is present as Fe^0 after reduction. However, the value of the additional consumption is within the experimental error. The evaluation of a subsequent temperature programmed desorption spectrum (TPD) which is not shown here, reveals high dispersion of the Rh^0 (H/Rh = 0.78 see Table 2).

Figure 2a shows the TPR-spectrum of Rh/NaY_{neutr} after calcination up to 500°C which was prepared by stirring reduced Rh/NaY in H_2O at pH = 5. The peak position around 50°C as well as the hydrogen consumption of H/Rh = 3.1 indicates full reduction of Rh_2O_3 present after calcination to metallic Rh. Figure 2c shows the TPR pattern of $RhFe/NaY_{neutr}$ which was obtained by a second ion exchange of prereduced Rh/NaY with Fe^{2+}. Rh_2O_3 reduction occurs at slightly higher temperatures (60°C) compared to the monometallic case (Fig. 2a). The iron reduction has been shifted from 350°C in the monometallic case (see Fig. 2b which represents the same pattern as Fig. 1b but is being shown for better comparison). With the total hydrogen consumption of H/(Rh + Fe) = 2.21, the atomic ratio Rh/Fe = 0.716 (Table 1) and with the assumption of H/Rh = 3 the obtained ratio of H/Fe = 1.64 indicates that 32% of the iron has been reduced to the metallic state whereas the rest is present as Fe^{2+} after reduction. As in the case of RhFe/NaY, the hydrogen

TABLE 2

Hydrogen Adsorption Capacity Obtained from Integration up to 350°C of TPD Profiles (TPD Profiles Not Shown)

Sample	RhFe/NaY	$RhFe/NaY_{neutr}$	$RhFe/NaY_{NaOH}$
H/Rh	0.78	0.70	0.89

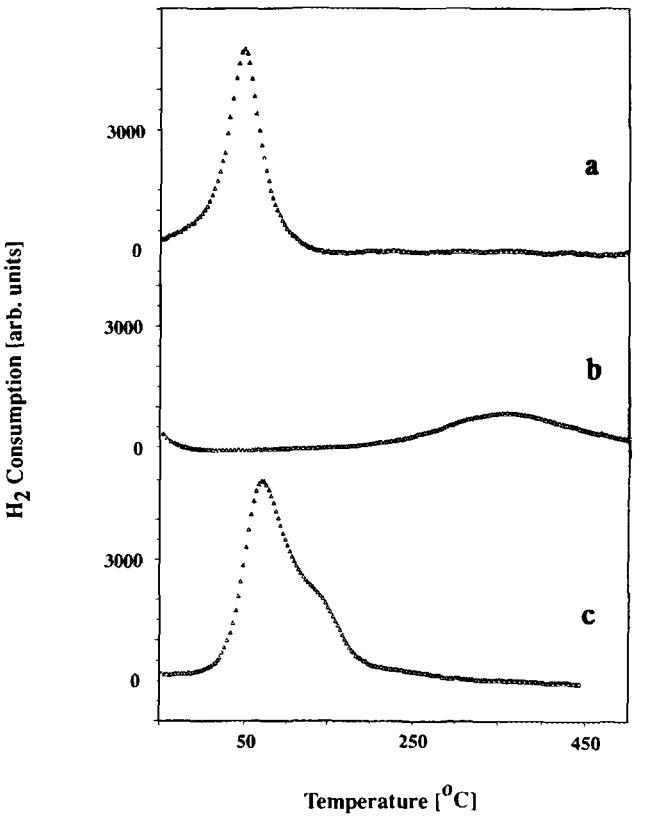

FIG. 2. TPR of Rh/NaY_{neutr} (a), Fe/NaY (b), and $RhFe/NaY_{neutr}$ (c) after calcination up to 500°C.

adsorption capacity of H/Rh = 0.70 indicates high metal dispersion.

Figure 3a displays the TPR-spectrum of R/NaY_{NaOH} after calcination up to 500°C, which was prepared by washing reduced Rh/NaY in H_2O at pH = 11. Again, the reduction peak at 50°C represents the reduction of rhodium oxide. The ratio H/Rh = 3.5 (Table 1) indicates the presence not only of Rh_2O_3 but also of RhO_2 which was recently identified in Rh/NaY after calcination up to 380°C (26). The integration of the TPR spectra of the NaOH treated Fe/NaY_{NaOH} (Fig. 3b) with broad peaks around 260 to 350°C yields to the ratio of H/Fe = 0.88 which might be interpreted by the reduction of Fe_2O_3 formed after calcination. The reduction profile of $RhFe/NaY_{NaOH}$ (Fig. 2c) exhibits beside the dominant peak at 60°C, representing the reduction of rhodium oxide to rhodium metal, a significant decrease to 150°C in the iron reduction temperature from 350°C in case of Fe/NaY_{NaOH}. This behavior is similar to that of $RhFe/NaY_{neutr}$ (Fig. 2c). The shoulder near 150°C may represent the reduction of Fe_2O_3. The total hydrogen consumption of H/(Rh + Fe), the ratio Rh/Fe + 0.81 (Table 1) and the assumption of H/Rh = 3 leads to a ratio of H/Fe = 2.48 meaning that 74% of the iron is present as Fe^0 after reduction.

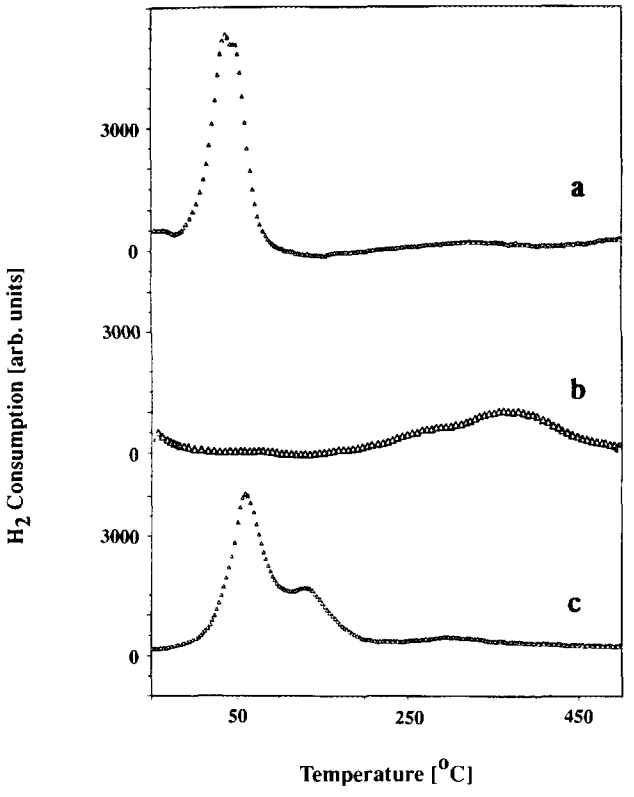

FIG. 3. TPR of Rh/NaY_{NaOH} (a), Fe/NaY_{NaOH} (b), and $RhFe/NaY_{NaOH}$ (c) after calcination up to 500°C.

Alternatively, the TPR of Rh/NaY_{NaOH} indicates the presence of Rh^{4+}, and the assumption H/Rh = 4 results in H/Fe = 1.7, corresponding to 35% Fe^0 present after reduction. Thus, it can be concluded from TPR that 35–74% of the iron is in the metallic state after the reduction of $RhFe/NaY_{NaOH}$. This value is outside experimental error. A slightly higher hydrogen adsorption per Rh is found with $RhFe/NaY_{neutr}$ compared to RhFe/NaY, see Table 2, H/Rh = 0.89.

3.2. FTIR

Three types of information of relevance to the objective of this study are obtained by IR spectroscopy. (1) The interaction of zeolite supported Rh clusters with carbon monoxide gives rise to a variety of carbonyl complexes, including the cation $Rh(CO)_2^+$ and the clusters $Rh_4(CO)_{12}$ and $Rh_6(CO)_{16}$. Their IR spectra have been fully assigned, see Refs. (30, 32, 33). In the present work, the band intensities after different pretreatment procedures are compared. (2) Upon reduction of Fe to Fe^0 and CO admission at low temperature, $Fe(CO)_5$ is formed which exhibits characteristic strong IR bands. Their observation thus proves reduction to Fe^0. (3) Changes in proton concentration are followed by monitoring the O–H stretching bands.

OH-Stretching region. Figure 4 shows the OH-stretching region of RhFe/NaY (4a), $RhFe/NaY_{neutr}$ (4b), and $RhFe/NaY_{NaOH}$ (4c) after reduction in H_2 up to 500°C. RhFe/NaY (4a) exhibits bands at 3640 and 3550 cm^{-1}, attributable to supercage and sodalite OH-groups created after the reduction of metal ions in the zeolite (24). The proton content after reduction of $RhFe/NaY_{neutr}$ is much lower, as manifest by a much smaller OH-band intensity (Fig. 4b), because the protons created after the rhodium reduction of Rh/NaY were re-exchanged during the preparation of $RhFe/NaY_{neutr}$ with Fe^{2+}. Also $RhFe/NaY_{NaOH}$ (Fig. 4c) reveals no peak in the OH-band region; here the protons created during the reduction of the metal have been re-exchanged with Na^+ ions during the NaOH treatment.

CO-FTIR: (RhFe/NaY). Figure 5a shows the CO-stretching region of RhFe/NaY after reduction, exposure to CO at room temperature and a subsequent He purge for 5 min: The strong band at 1827 cm^{-1} indicates the presence of Rh_6CO_{16} clusters which are present in the form of the $Rh_6(CO)_{12}(\mu_2\text{-}CO)_4$-configuration. The bands at 1871 (w), 2068 (s), and 2093 (s) cm^{-1} can also be attributed to this species and may be compared to those found by Rao *et al.* (32) (Table 3). The band at 2021 cm^{-1} can be assigned to the *gem*-dicarbonyl Rh ion, $Rh^+(CO)_2$, coordinated to zeolite oxygens. These species also exhibit a shoulder at 2098 cm^{-1} which is superimposed by the strong band at 2093 cm^{-1}. The bands at 2117 and 2053 cm^{-1} may represent $Rh^+(CO)_2$ coordinated to a zeolite proton and one framework oxygen (27, 30). The band at 2195 cm^{-1} is characteristic for CO adsorbed on Fe^{2+} in NaY (9). Furthermore, small broad bands occur at 1945 and 1985 cm^{-1}. These bands are absent in the case of CO

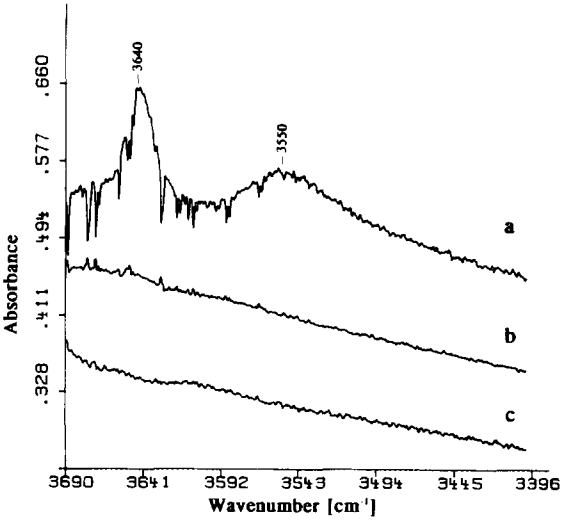

FIG. 4. OH-stretching region of RhFe/NaY (a), $RhFe/NaY_{neutr}$ (b), and $RhFe/NaY_{NaOH}$ (c) after reduction up to 500°C.

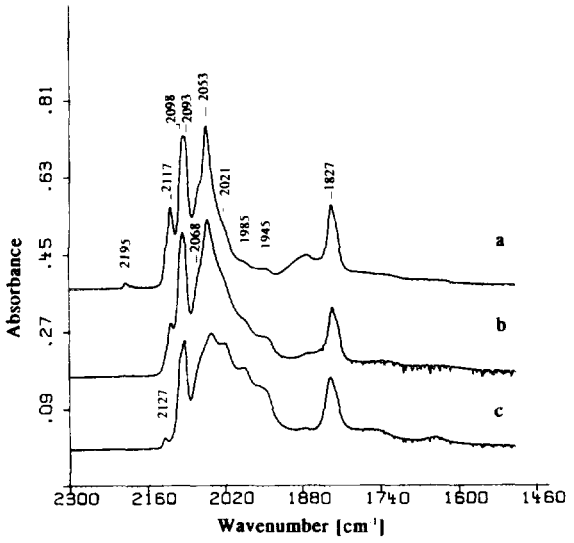

FIG. 5. FTIR-spectra of RhFe/NaY (a), RhFe/NaY_{neutr} (b), and RhFe/NaY_{NaOH} (c) after 10 min CO treatment at room temperature and a flow of 30 ml/min and subsequent 6 min He purge. The contributions of the NaY framework are subtracted.

adsorbed on monometallic NaY supported Rh (26, 32) and are characteristic for $Fe(CO)_5$ (34, 35), in the supercages of NaY (Table 3). The existence of subcarbonyls such as $Fe(CO)_4$ cannot be excluded (35). The observed iron carbonyl species may also possess bands at 2122, 2060, 2043, 2015, and 1960 cm^{-1} which are hidden under the more intense Rh carbonyl bands. The presence of iron carbonyl after CO admission shows the presence of small amounts of metallic iron after hydrogen reduction, as already indicated by the TPR analysis of RhFe/NaY.

TABLE 3

Literature Data of IR Stretching Frequencies for Rhodium and Iron Carbonyl Species in Zeolite NaY

Species	Wavenumbers (cm^{-1})	Reference
$Rh_6(CO)_{16}(\mu_2\text{-}CO)_4$	2092 s, 2072 s, 2060 w, 1872 w, 1830 s	(32)
$Rh^+(CO)_2$ (coord. to $2O_z$) (coord. to O_z and O_zH^+)	2098 s, 2022 s 2114 s, 2048 s	(32, 26, 30)
$Fe(CO)_5$	2122 w, 2060 s, 2044 s, 2012 s, 1985 s, 1960 sh, 1945 s	(34, 35)
$Rh_4(CO)_{12}$	2082 s, 2032 w, 1876 w 1835 s	(32)

(*RhFe/NaY_{neutr}*). No bands besides those observed with RhFe/NaY after admission of CO, are detected with RhFe/NaY_{neutr} (Fig. 5b). However, differences in band intensities are recognizable: an increase in the iron carbonyl bands at 1945 and 1985 cm^{-1} with respect to the rhodium carbonyl bands indicates a higher percentage of metallic iron present in RhFe/NaY_{neutr} compared to RhFe/NaY. Also, the band at 2117 cm^{-1} representing $Rh^+(CO)_2$ coordinated to zeolitic protons, has decreased considerably as expected since the protons generated during the reduction of the Rh have been exchanged against Fe^{2+} leading to a drastic decrease in proton content of RhFe/NaY_{neutr}.

(*RhFe/NaY_{NaOH}*). Fig. 5c shows the CO-FTIR spectrum of RhFe/NaY_{NaOH}. A remarkable increase in the intensity of the bands at 1945 and 1986 cm^{-1} indicative for $Fe(CO)_5$ can be observed. In addition bands at 1955 and 2127 cm^{-1} appear, also indicative for $Fe(CO)_5$ in NaY (Table 3). These bands were hidden before under the intense rhodium carbonyl bands. No band at 2117 cm^{-1} characteristic for $Rh^+(CO)_2$ coordinated to zeolitic protons is observed, leading to the conclusion that the intense band at 2043 cm^{-1} cannot be attributed to $Rh^+(CO)_2$ coordinated to zeolitic protons, but to $Fe(CO)_5$ according to Table 2. The band at 2021 cm^{-1} has also increased considerably with respect to RhFe/NaY and RhFe/NaY_{neutr}. Since the intensity of the band at 2098 cm^{-1} characteristic for $Rh^+(CO)_2$ coordinated to zeolitic oxygens has not increased significantly, the strong increase in the band at 2021 cm^{-1}, characteristic for both the rhodium and the iron carbonyl species has to be attributed to $Fe(CO)_5$. This result indicates a higher Fe^0 content of RhFe/NaY_{NaOH}, compared to RhFe/NaY and RhFe/NaY_{neutr}.

3.3. *Ferromagnetic Resonance (FMR)*

Figure 6 shows the FMR-spectra of the samples RhFe/NaY (6a) and RhFe/NaY_{neutr} (6b). No ferromagnetic resonance has been observed for these samples. The signal at 3000 G is due to Mn impurities of the zeolite matrix itself. Only RhFe/NaY_{NaOH} (Fig. 6c) exhibits a strong temperature-dependent ferromagnetic resonance signal, indicating superparamagnetic particles consisting of a single ferromagnetic domain (36). The temperature dependent signal exhibits an isosbestic point at 3220 G corresponding to a g-value of 2.02, a value similar to that found for Fe^0 clusters in NaX (37). We therefore assign the FMR-signal to a Fe^0 phase. The monometallic Fe/NaY_{NaOH} sample shows no strong ferromagnetic signal (Fig. 6d), indicating that the majority of the iron in this sample is not present in form of Fe^0 after reduction, as already shown by the hydrogen consumption of H/Fe = 0.88 in the TPR analysis. The observed broad signal might be due to traces of Fe^0 in the sample. The presence of an

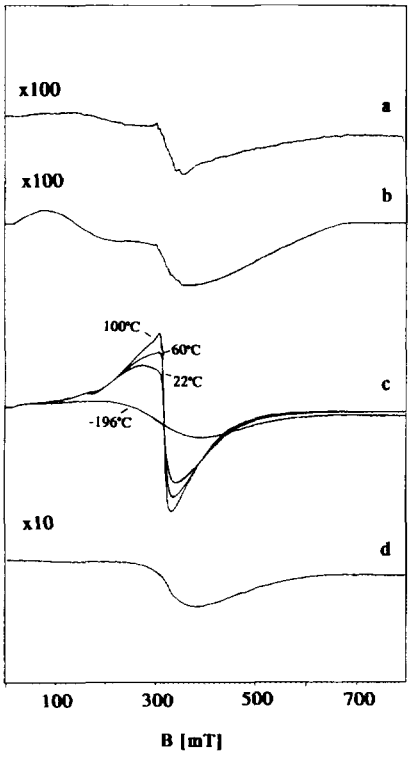

FIG. 6. FMR-spectra obtained at room-temperature of RhFe/NaY (a), RhFe/NaY_{neutr} (b), and Fe/NaY_{NaOH} (d) as well as temperature dependent spectra of RhFe/NaY_{NaOH} (c) after reduction up to 500°C.

Fe^0 phase in RhFe/NaY_{NaOH} can only be explained by alloy formation, because the monometallic Fe/Nay_{NaOH} exhibits no FMR signal characteristic for Fe^0 clusters. RhFe alloys with an iron content less than 50 at.% are antiferromagnetic, and no strong FMR signal should be observed (39). Therefore, we attribute the FMR signal of RhFe/NaY_{NaOH} to RhFe-clusters with an Fe content >50 at.%.

3.4. *Mössbauer Spectroscopy*

Mössbauer spectra obtained at room temperature after in-situ reduction up to 500°C are shown in Fig. 7. RhFe/NaY (Fig. 7a) exhibits two doublets, which are further denoted as inner and outer doublet respectively. Both doublets exhibit Mössbauer parameters (Table 4) characteristic for NaY supported Fe^{2+}. The outer doublet has been assigned to Fe^{2+} in the hexagonal prisms of the NaY (site I) and the inner doublet to Fe^{2+} at sites I′, II′, and/or II (40). In addition a singlet with IS = -0.05 ± 0.04 mm/s is needed to fit the data. This singlet can be attributed to Fe^0, either in the superparamagnetic state (36) and/or in a fcc-RhFe alloy (42). Similar isomer shifts have been reported by Ichikawa *et al.* for RhFe particles on SiO_2 (15). It follows from the relative area of this peak that 6% of the iron is present as Fe^0. It is important to note that our strategy for fitting the Mössbauer spectra of this study was to use spectral components having Mössbauer parameters with values reported in previous studies of related systems, e.g., (40, 41, 43).

The spectrum of RhFe/NaY_{neutr} is shown in Fig. 7b. The outer doublet can be attributed to Fe^{2+} in the hexagonal prisms of Y zeolite (site I), as observed in the RhFe/NaY sample. Furthermore, the Fe^{2+} inner doublet observed in the RhFe/NaY sample is absent and a new doublet has emerged with IS = 0.37 mm/s and QS = 0.90 mm/s. The additional doublet has Mössbauer parameters similar to those observed by others. Bartholomew and Boudart (1) as well as Garten *et al.* (3), attributed this doublet for PtFe/SiO_2 samples to zerovalent iron in a highly unsymmetrical environment on the surface of alloy

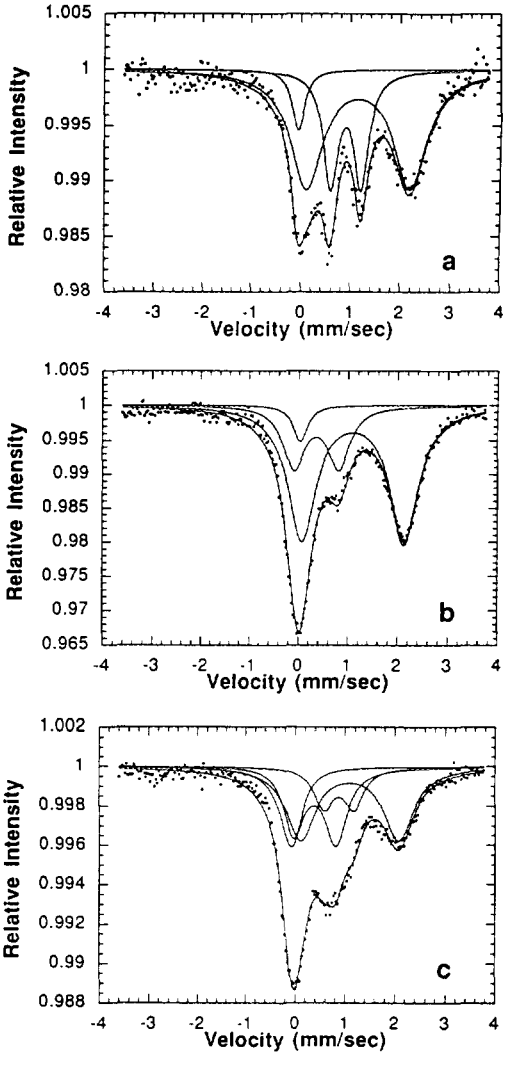

FIG. 7. Mössbauer spectra of RhFe/NaY (a), RhFe/NaY_{neutr} (b), and RhFe/NaY_{NaOH} (c) after reduction up to 500°C.

TABLE 4

Mössbauer Parameters of the Spectra Shown in Fig. 7

Sample	IS (mm/s)	QS (mm/s)	Line width (mm/s)	Rel. area (%)	Species
RhFe/NaY	0.91	0.61	0.36	29	Fe^{2+}
	1.16	2.08	0.78	65	Fe^{2+}
	−0.05	—	0.30	6	Rh–Fe alloy
$RhFe/NaY_{neutr}$	0.37	0.9	0.53	25	Fe^{3+} or Fe^0
	1.11	2.06	0.69	70	Fe^{2+}
	0.04	—	0.36	5	Rh–Fe alloy
$RhFe/NaY_{NaOH}$	0.37	0.90	054	32	Fe^{3+} or Fe^0
	1.09	1.97	0.71	40	Fe^{2+}
	0.88	0.60	0.48	14	Fe^{2+}
	−0.03	—	0.47	14	Rh–Fe alloy

particles, whereas Niemantsverdriet *et al.* (4) and Ichikawa *et al.* (11) assumed that this doublet represents irreducible Fe^{3+}. We attribute this doublet to zerovalent iron, as will be shown below. Also, a singlet with IS = 0.04 mm/s attributed to Fe^0 is observed with a relative area of only 5%.

The Mössbauer spectrum of $RhFe/NaY_{NaOH}$ after reduction is shown in Fig. 7c. This rather complex spectrum could be fit using combinations of the singlets and doublets observed in Figs. 7a and 7b. Two of the doublets are consistent with the inner and outer doublets of Fe^{2+} observed in the RhFe/NaY sample of Fig. 7a. The additional doublet with IS = 0.37 mm/s and QS = 0.09 mm/s corresponds to the zerovalent iron doublet observed in the reduced $RhFe/NaY_{neutr}$ sample. In addition, the singlet with IS = 0.03 mm/s indicates the presence of Fe^0. The relative area of this singlet is only 14%, which is much below the amount of metallic iron found by TPR for this sample.

The results of the TPR-analyses suggest that 32% of the Fe is reduced to Fe^0 for the $RhFe/NaY_{neutr}$ sample. These results suggest that the additional doublet with IS = 0.37 mm/s and QS = 0.90 mm/s in the Mössbauer spectra of the samples corresponds to zerovalent iron. Unambiguous proof for this statement has been obtained from Mössbauer spectroscopic data in combination with separate research where $Fe(CO)_5$ was decomposed onto prereduced RhFe/NaY under flowing H_2/Ar to prepare Fe^0 in close contact with Rh^0 clusters (23). In that work no Fe^{2+} could be detected by Mössbauer spectroscopy, but a doublet with IS = 0.39 mm/s and QS = 0.90 mm/s was very pronounced and was attributed to Fe^0 alloyed to Rh. Therefore, the observation of the same doublet in the present, thoroughly reduced samples is considered conclusive evidence for the presence of this species, as will be discussed below.

3.5. *Transmission Electron Microscopy (TEM)*

Electron micrographs of RhFe/NaY, $RhFe/NaY_{neutr}$, and $RhFe/NaY_{NaOH}$ are shown in Figs. 8a, 8b, and 8c. The obtained lattice fringes represent the (111) planes of the NaY support with a lattice spacing of 1.3 nm. No metal particles on the surface of the zeolite matrix could be detected. The micrographs of RhFe/NaY and $RhFe/NaY_{neutr}$ exhibit no particles larger than the supercages (1.3 nm). In contrast, $RhFe/NaY_{NaOH}$ shows also some particles inside the zeolite matrix with diameters of 2–4 nm.

3.6. *CO Hydrogenation Catalysis*

Selectivity data for RhFe/NaY and $RhFe/NaY_{neutr}$ are presented in Figs. 9a and 9b. Both RhFe/NaY and $RhFe/NaY_{neutr}$ produce mainly CH_4 and higher hydrocarbons. Only traces of oxygenates (around 1%, mainly acetaldehyde and ethanol) could be detected in the product stream of both samples. In contrast, $RhFe/NaY_{NaOH}$ produces oxygenates with 20% selectivity (Fig. 9c). The selectivity toward CH_4 is similar to that of RhFe/NaY and $RhFe/NaY_{neutr}$, whereas the selectivity toward higher hydrocarbons decreased. The selectivity toward different oxygenate products is shown in Fig. 10. The dominant product is ethanol (13% selectivity), followed by diethylether (7%) and ethylacetate which appears, however, only after a long induction period and is produced in amounts comparable to diethylether after 400 min time on stream. The selectivity towards methanol is near 1%. The turnover frequencies, based on the H/Rh ratio measured before the catalytic run, are shown in Fig. 11 versus time on stream. Both, $RhFe/NaY_{neutr}$ and $RhFe/NaY_{NaOH}$ show higher turnover frequencies ($6–7 \times 10^{-3}$ s^{-1}) than RhFe/NaY ($4–5 \times 10^{-3}$ s^{-1}) during the first hours of the catalytic runs. As more Fe^0 is present in $RhFe/NaY_{neutr}$ and RhFe/

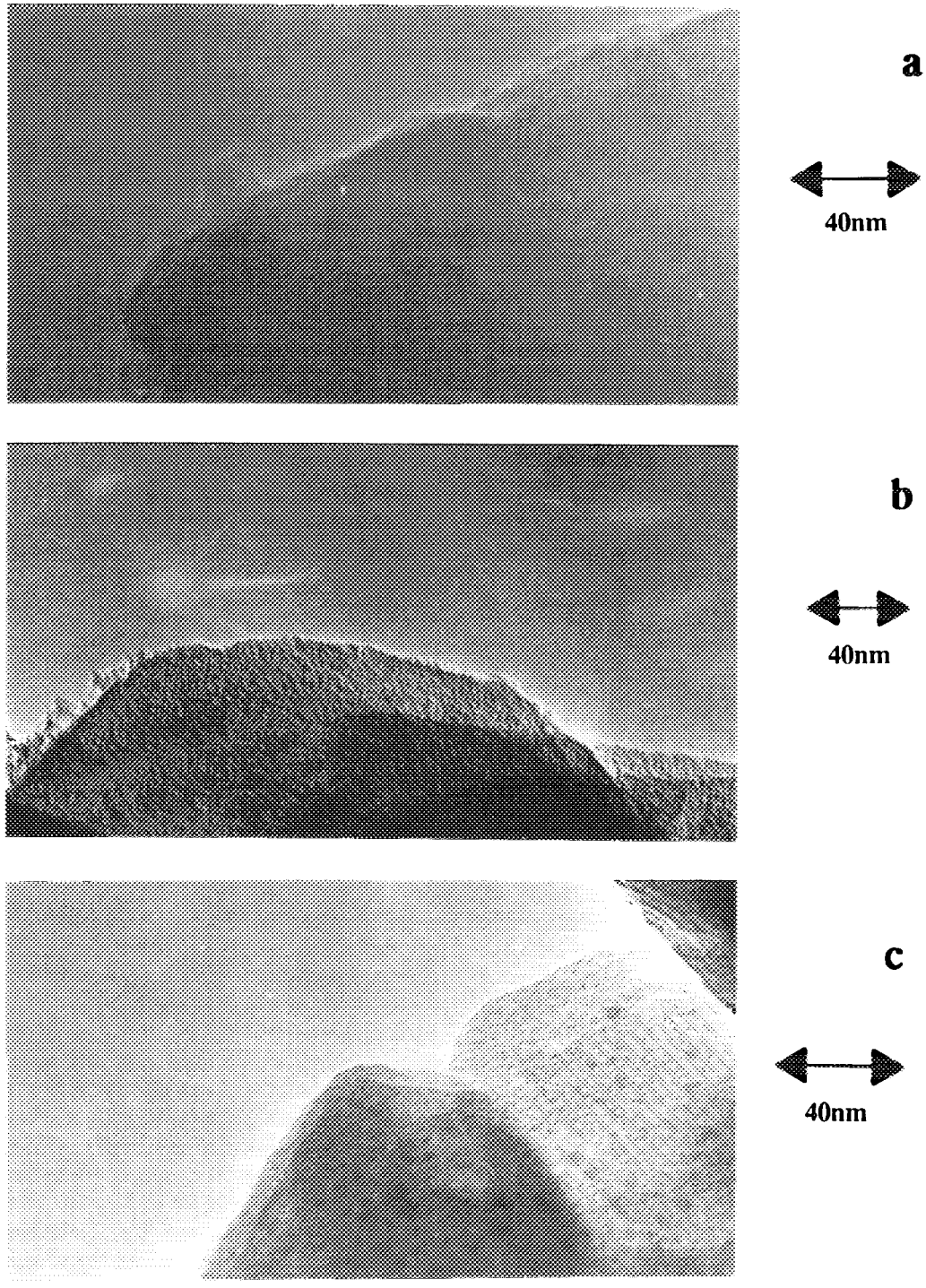

FIG. 8. TEM micrographs of RhFe/NaY (a), RhFe/NaY_{neutr} (b), and RhFe/NaY_{NaOH} (c).

NaY_{NaOH} after reduction, it is probable that Fe^0 is the cause of the enhanced activity, because Fe^0 is known to dissociate better CO than Rh^0 does (22). Electron micrographs after reaction are shown in Fig. 12. All samples show the presence of 5–10 nm particles at the outside of the zeolite support. However, the particle size does not significantly differ for RhFe/NaY, RhFe/NaY_{neutr} and RhFe/NaY_{NaOH}.

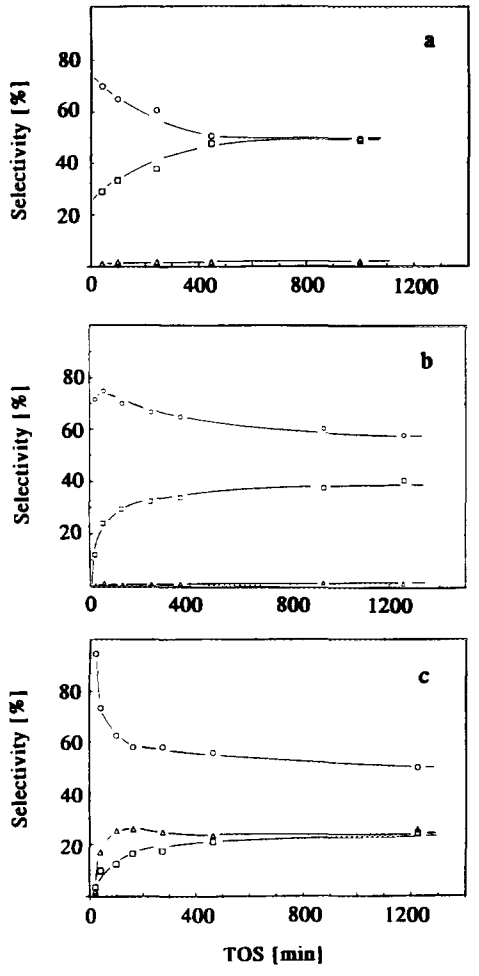

FIG. 9. Selectivity of RhFe/NaY (a), RhFe/NaY_{neutr} (b), and RhFe/NaY_{NaOH} (c).

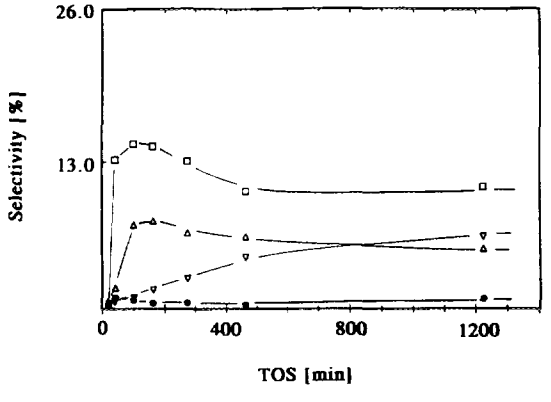

FIG. 10. Product selectivity toward different oxygenates of RhFe/NaY_{NaOH}.

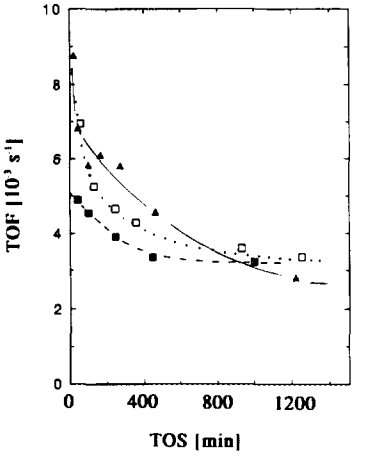

FIG. 11. Conversion of CO versus time on stream for RhFe/NaY (a), RhFe/NaY_{neutr} (b), and RhFe/NaY_{NaOH} (c).

4. DISCUSSION

4.1. Alloy Formation and Extent of Iron Reduction

Fe^{2+} ions in Fe/NaY are not reducible to Fe^0 as reported by Boudart *et al.* (44) and Balse *et al.* (45) on the basis of Mössbauer spectroscopy. This is confirmed by the present TPR results of the monometallic Fe/NaY. In the case of RhFe/NaY where the Rh can be reduced to the metallic state, the present TPR and Mössbauer spectroscopy results indicate that a small but significant amount of Fe (3–5%) is also reduced to the metallic state. A similar effect has been reported previously for the systems PdFe/NaY (9) and PdNi/NaY (46). The fact that iron is reduced to Fe^0 suggests alloy formation. Once the rhodium has been reduced to the metallic state it is able to dissociate hydrogen; these H atoms can reduce Fe^{3+} or Fe^{2+} ions, that are in close contact with the Rh particle, to Fe^0, which results in alloy formation. The presence of Rh clusters covered with hydrogen leads to a shift of the iron reduction peak in the TPR pattern to lower temperatures, which is observed for RhFe/NaY and even more for RhFe/NaY_{neutr} and RhFe/NaY_{NaOH}, indicating close proximity of iron and rhodium.

The presence of Fe^0 has also been detected in reduced RhFe/NaY_{neutr}. TPR analysis indicates that 32% of the iron is reduced to Fe^0 and the rest is present as Fe^{2+}. This result would be in contradiction to the Mössbauer spectroscopy data if the assignment proposed by Niemantsverdriet (4) and Ichikawa (11) is applied. However, agreement of TPR and Mössbauer data is achieved, if the signal assignment proposed by Boudart *et al.* (1) and Garten *et al.* (2) is accepted. We have examined the question of the interpretation of the Mössbauer data in a separate study, described in Ref. (23). In brief we found that

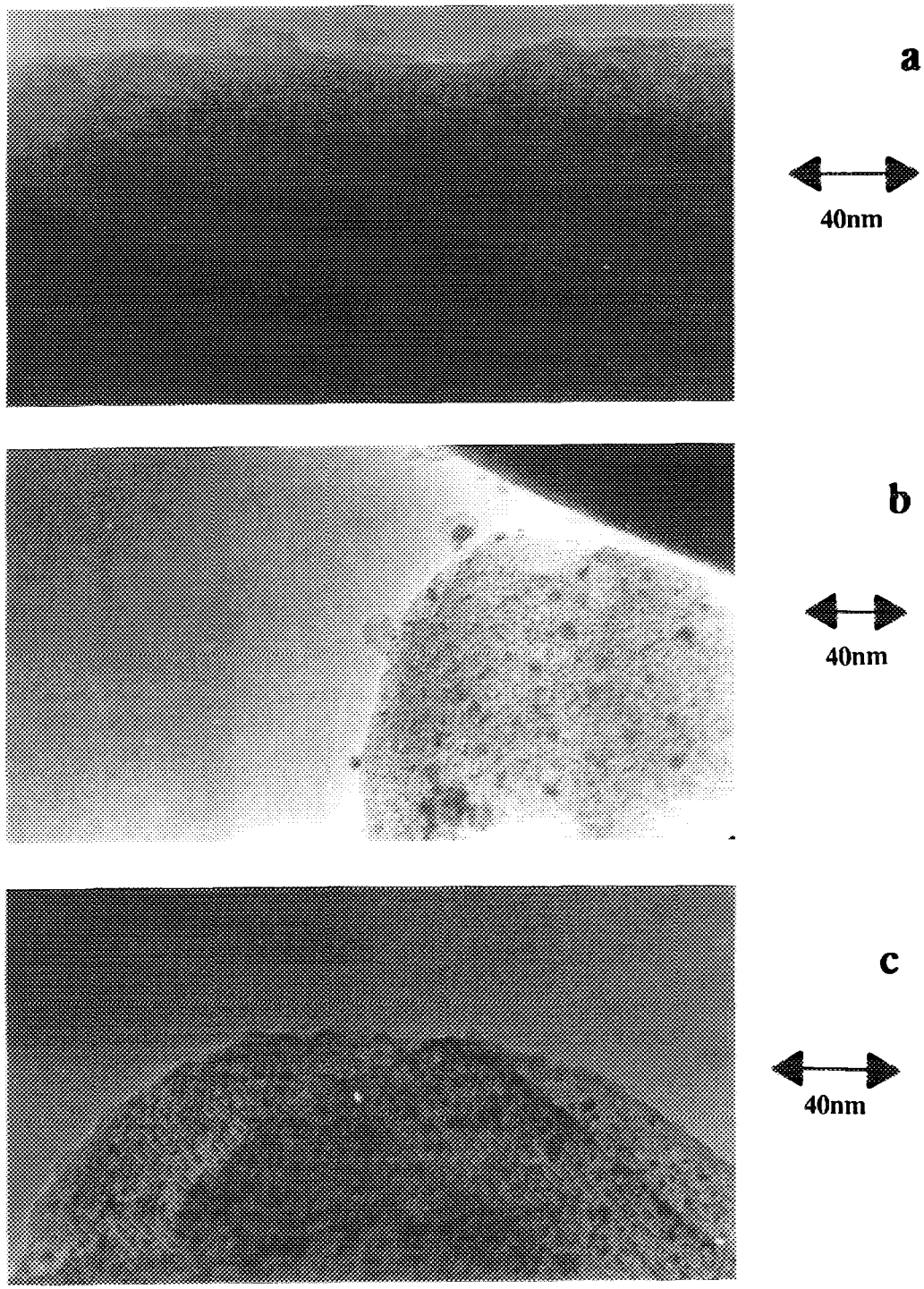

FIG. 12. TEM micrographs of RhFe/NaY (a), RhFe/NaY_{neutr} (b), and RhFe/NaY_{NaOH} (c) after CO-hydrogenation reactions.

experiments in which Fe was added to RhFe/NaY by decomposing $Fe(CO)_5$ followed by reductive treatment in H_2, gave Mössbauer spectra which confirmed the absence of unreduced Fe^{2+} and Fe^{3+}, but the same doublet is found as by the other authors. On the basis of this work and supporting XPS evidence, we assign this doublet to Fe^0 in the reduced catalyst. With this assignment there is full agreement of the present Mössbauer spectroscopy and TPR data. Moreover, the TPR data show that RhFe/NaY_{NaOH} should have the highest Fe^0 content of

35–72%, depending on the assumed $RhO_2/Rh_2/O_3$ ratio (see Results section). This trend is confirmed by the strong FTIR intensity of the $Fe(CO)_5$ bands in comparison to RhFe/NaY and $RhFe/NaY_{neutr}$ (Fig. 4). Mössbauer analysis shows only 14% of the spectral area is due to the Fe^0 singlet. The TPR result of 35–74% Fe^0 is matched by the Mössbauer data if the disputed doublet is assigned to Fe^0 on the surface of $RhFe_x$ particles. This assignment leads to a total Fe^0 content of 46%.

Upon accepting the result that 74% of the Fe is reduced to Fe^0, i.e. the maximum possible compatible with the TPR data, it follows that the average particle composition is Rh/Fe = 1/1 in $RhFe/NaY_{NaOH}$. FMR shows a strong temperature dependent signal indicating supraparamagnetic particles with a Fe^0 content >50 at.%. Presumably, there is a broad distribution of the composition of the individual $RhFe_x$ particles around the average value. On the other hand, RhFe/NaY and $RhFe/NaY_{neutr}$ show no FMR signal indicating a low Fe^0 content. This result is in agreement with the TPR analysis that shows a nominal relative composition of $Rh^0 : Fe^0 = 27 : 1$ for RhFe/NaY and of $Rh^0 : Fe^0 = 2 : 1$ for $RhFe/NaY_{neutr}$. The former ratio represents Fe^0 diluted in a Rh matrix which is not ferromagnetic (47) and the latter might indicate a RhFe alloy with CsCl structure which is antiferromagnetic. None of these cases can give an FMR signal (39, 47) This behavior is different from that of PdFe/NaY, where it has been found that one Fe atom suffices to polarize the surrounding Pd matrix in a cluster leading to a strong FMR signal (9). Indeed it is known that Pd is much easier to polarize by Fe impurities than Rh (47).

4.2. *Behavior under CO Atmosphere: Carbonyl Formation*

After exposure to CO at room temperature, bands typical for rhodium carbonyls ($Rh^+(CO)_2$ and $Rh_6(CO)_{12}(\mu_2\text{-}CO)_4$) as well as iron carbonyls ($Fe(CO)_5$) are observed. This behavior is different from PdFe/NaY where no formation of iron carbonyls could be detected (9). It is well known that Rh clusters disintegrate under CO atmosphere; even Rh^0 clusters with more than six Rh atoms form rhodium carbonyl species upon adsorption of CO (26, 32, 48). The same behavior is observed with RhFe/NaY. Once Rh carbonyls start to form, the remaining Fe^0 of the alloy cluster is converted into $Fe(CO)_5$ in the CO atmosphere. Since reduction of Fe^{2+} to Fe^0 by CO at room temperature is highly improbable the amount of $Fe(CO)_5$ is likely to be indicative for the amount of Fe^0 present, as discussed above. If one then compares the relative line intensities of the Rh and Fe carbonyl species, it follows that the Fe^0 content is the lowest in RhFe/NaY, it is higher in $RhFe/NaY_{neutr}$ and highest in $RhFe/NaY_{NaOH}$. This trend supports the TPR results and thus also our assignment of the doublet in the Mössbauer spectrum.

4.3. *CO-Hydrogenation*

The catalytic signature of reduced RhFe/NaY in CO hydrogenation is similar to that of RhMn/NaY (16): the selectivity toward oxygenates is low before protons are neutralized. Also a remarkable decrease in proton concentration in the $RhFe/NaY_{neutr}$ does not lead to an increase in the selectivity toward oxygenates. This result indicates that naked Fe^{2+} ions in RhFe/NaY do not serve as promoters for the formation of oxygenates. In contrast, $RhFe/NaY_{NaOH}$ exhibits high selectivity toward oxygenates, especially ethanol.

From the above results and discussion it follows that the catalyst which shows highest selectivity for oxygenates, $RhFe/NaY_{NaOH}$, does not contain Fe^{3+} after reduction. The present results thus do not support the view that an irreducible Fe^{3+} species is the promoter responsible for directing CO hydrogenation towards oxygenates, as had been suggested by others (19). The present results rather suggest that the selectivity promoting iron is in the oxidation state of Fe^{2+}. Treatment of the catalysts precursor in NaOH will convert Fe^{2+} ions into $Fe(OH)_2$, which will lose water and be converted to Fe_2O_3 during calcination. Reduction of this oxide in macroscopic system is known to proceed via Fe_3O_4 to FeO to Fe^0. In highly dispersed systems and in the absence of a metal which catalyzes the reduction, such as rhodium, virtually no Fe^0 is formed, as reported by us for Fe/NaY (9) and by Wielers *et al.* for Fe/SiO_2 (49). Even 6 h reduction of a Fe/SiO_2 catalyst at 550°C led predominantly to Fe^{2+}. These authors interpret their Mössbauer spectra by assuming that a highly dispersed Fe^{2+} oxide and a Fe^{2+} silicate phase are formed, of which the latter is assumed to give the doublet with QS = 1.85 mm/s (49). In the present study, the Mössbauer spectrum of $RhFe/NaY_{NaOH}$ exhibits Fe^{2+} doublets suggesting that after reduction of $RhFe/NaY_{NaOH}$ highly dispersed Fe^{2+} oxide is formed. This appears to act as a *selectivity promoter*, favoring formation of oxygenates. It is interesting that with the Fe or Mn promoted Rh catalysts ethanol is predominant among the oxygenates, whereas with Fe promoted Pd catalysts methanol prevails (24, 25).

The presence of Fe^0 seems to increase the turnover frequency (TOF), calculated per Rh^0. $RhFe/NaY_{neutr}$ and $RhFe/NaY_{NaOH}$ have a higher Fe^0 content than RhFe/NaY and show enhanced activity in CO hydrogenation during the first hours. It thus appears that Fe^0 acts as an *activity promoter*.

All catalysts exhibit particle growth during CO hydrogenation; particles with diameters from 5–10 nm are located partly on the outside of the zeolite support (Fig. 12). The

particle growth might have occurred via the formation of metal carbonyls during the CO hydrogenation reaction. Adsorption of CO at room temperature converts most of the metal into different rhodium carbonyl species as well as $Fe(CO)_5$ (as discussed above). The formation of carbonyl species could weaken the metal–support interaction which leads to the agglomeration of the metal to the zeolite surface under syngas conditions.

5. CONCLUSIONS

The presence of Rh in RhFe/NaY leads to formation of Fe^0 in RhFe clusters upon reduction in H_2 at 500°C. This behavior matches that of PdFe/NaY and similar bimetal pairs. Upon CO admission at room temperature, the bimetallic clusters disproportionate to carbonyls, including $Rh_6(CO)_{12}(\mu_2\text{-}CO)_4$, $Rh^+(CO)_2$, $Fe(CO)_5$ and/or iron subcarbonyls; the relative abundancies of these products depend on the proton content of the sample. Treatment in NaOH of a pre-reduced RhFe/NaY sample, followed by calcination and reduction, maximizes the Fe^0 content of the bimetallic clusters, some of which contain >50 at.% Fe and show a superparamagnetic FMR signal. During CO hydrogenation, iron exerts two promoting functions: Fe^0 alloyed to Rh increases the turnover frequency, acting as *activity promoter;* a highly dispersed Fe^{2+} oxide in contact with Rh particles promotes the *selectivity* toward oxygenates, in particular ethanol and ethyl acetate. In the presence of Fe^{2+} ions, but the absence of Fe^{2+} oxide, the selectivity towards oxygenates falls to almost zero. The results are at variance with an earlier hypothesis claiming that Fe^{3+} ions, surviving the reducing conditions of catalyst preparation and syngas catalysis, direct the Rh catalyzed conversion of CO + H_2 towards oxygenates.

ACKNOWLEDGMENTS

The authors gratefully acknowledge support from the Director of the Chemistry Division, Basic Energy Sciences, U.S. Department of Energy, Grant DE-FG02-87ER13654. We also thank Johnson Matthew, Ltd. for providing $RhCl_3$ in their precious metal loan program.

REFERENCES

1. Bartholomew, H., and Boudart, M., *J. Catal.* **29,** 278 (1974).
2. Garten, R. L., *in* "Mössbauer Effect Methodology" (I. J. Gruverman, Ed.), Vol. 10, p. 69, Plenum, New York, 1976.
3. Lam, Y. L., and Garten, R. L., "Proceedings of the 6th Ibnero-American Symposium on Catalysis" (Rio de Janeiro, 1978).
4. Niemantsverdriet, J. W., van der Kraan, A. M., and Delgass, W. N., *J. Catal.* **89,** 138 (1984).
5. Niemantsverdriet, J. W., Aschenbeck, D. P., Fortunato, F. A., and Delgass, A. M., *J. Mol. Catal.* **25,** 285 (1984).
6. Van't Blik, H. F. J., and Niemantsverdriet, J. W., *Appl. Catal.* **10,** 155 (1984).
7. Niemantsverdriet, J. W., van Kaam, J. A. C., Flipse, C. F. J., and van der Kraan, A. M., *J. Catal.* **96,** 58 (1985).
8. Niemantsverdriet, J. W., van der Kraan, A. M., and Delgass, W. N., *J. Catal.* **89,** 138 (1984).
9. Xu, L., Lei, G.-D., Sachtler, W. M. H., and Cortright, R. D., Dumesic, J. A., *J. Phys. Chem.* **97**(44), 11517 (1993).
10. Guczi, L. *Catal. Lett.* **7,** 205 (1990).
11. Minai, Y., Tominaga, T., Fukushima, T., and Ichikawa, M., "Industrial Applications of the Mössbauer Effect" (G. J. Long and J. G. Stevens, Eds.) p. 635, Plenum, New York, 1986.
12. Sabatier, P., and Senderens, J. B., *C.R. Seances Acad. Sci.* 514 (1902).
13. Bhasin, M. M., Bartley, W. J., Ellgen, P. C., and Wilson, T. P., *J. Catal.* **54,** 120 (1978).
14. Fukoka, A., Kimura, T., Kosugi, N., Kuroda, H., Minai, Y., Sakai, Y., Tominaga, T., and Ichikawa, M., *J. Catal.* **126,** 434 (1990).
15. Ichikawaw, M., Fukuoka, A., and Kimura, T., *in* "Proceedings, 9th International Congress on Catalysis, Calgary, 1988" (M. J. Phillips and M. Ternan, Eds.), Vol. 2, p. 569. Chem. Institute of Canada, Ottawa, 1988.
16. Treviño, H., and Sachtler, W. M. H., *Catal. Lett.* **27,** 251 (1994).
17. Borer, A. L., Brönnimann, C., and Prins, R., *J. Catal.* **145,** 516 (1994).
18. Borer, A. L., and Prins, R., *J. Catal.* **144,** 439 (1993).
19. Fukuoka, A., Ichikawa, M., Hriljac, J. A., and Shriver, D. F., *Inorg. Chem.* **26,** 3643 (1987).
20. Biloen, P., and Sachtler, W. M. H., *Adv. Catal.* **30,** 165 (1980).
21. Sachtler, W. M. H., and Ichikawa, M. J., *J. Phys. Chem.* **90,** 4758 (1986).
22. Sachtler, W. M. H., "Proceedings, 8th International Congress on Catalysis, Berlin, 1984," p. 151. Dechema, Frankfurt-am-Main, 1984.
23. Schünemann, V., Treviño, H., Sachtler, W. M. H., Fogash, K., and Dumesic, J. A., *J. Phys. Chem.* **99**(4), 1317 (1995).
24. Choudary, B. M., Lázár, K., Bogyai, I., and Guczi, L., *J. Chem. Soc. Faraday Trans. I* **86,** 419 (1990).
25. Guczi, L., Lu, G., and Zsoldos, Z., *Catal. Today* **17,** 459 (1993).
26. Wong, T. T., Stakheev, A. Y., and Sachtler, W. M. H., *J. Phys. Chem.* **96**(19), 7735 (1992).
27. Wong, T. T. T., and Sachtler, W. M. H., *J. Catal.* **141,** 407 (1993).
28. Schünemann, V., Adelman, B., and Sachtler, W. M. H., *Catal. Lett.* **27,** 259 (1994).
29. Tomczak, D. C., Schünemann, V., Lei, G.-D., and Sachtler, W. M. H., *Microporous Materials,* in press.
30. Tomczak, D., Zholobenko, V., Treviño, H., Lei, G.-D., and Sachtler, W. M. H., "Zeolites and Related Microporous Materials: State of the Art 1994" (J. Weitkamp, H. G. Karge, H. Pfeifer, and W. Hölderich, Eds.) Studies in Surface Science and Catalysis, Vol. 84, p. 893, Elsevier, Amsterdam, 1994.
31. Huang, Y.-Y., and Anderson, J. R., *J. Catal.* **40,** 143 (1975).
32. Rao, L.-F., Fukuoka, A., Kosugi, N., Kuroda, H., and Ichikawa, M., *J. Phys. Chem.* **94**(13), 5317 (1990).
33. Beutel, T., Knözinger, H., Treviño, H., Zhang, Z. C., Sachtler, W. M. H., Dossi, C., Psaro, R., and Ugo, R., *J. Chem. Soc. Faraday Trans. I.* **90**(9), 1335 (1994).
34. Bowers, C., and Dutta, P. K., *J. Phys.Chem.* **93,** 2596 (1989).
35. Bein, T., and Jacobs, P. A., *J. Chem. Soc. Faraday Trans I* **79,** 1819 (1983).
36. Mørup, S., and Dumesic, J. A., and Topsøe, H., "Applications of Mössbauer Spectroscopy Vol II" (Cohen R. L., ed), p. 1. Academic Press, New York, 1980.

37. Ziethen, H. M., Winkler, H., Schiller, A., Schünemann, V., Trautwein, A. X., Quazi, A., and Schmidt, F., *Catal. Today* **8,** 427 (1991).
38. Shirane, G., Nathans, R., and Chen, C. W., *Phys. Rev.* **134,** A1547 (1964).
39. Okuda, K., Hirao, M., and Date, M., *J. Phys. Soc. Jpn.* **25,** 1735 (1968).
40. Delgass, W. N., Garten, R. L., and Boudart, M., *J. Phys. Chem.* **73,** 2970 (1969).
41. Aparicio, L. M., Dumesic, J. A., Fang, S.-M., Long, M. A., Ulla, M. A., Millman, W. S., and Hall, W. K., *J. Catal.* **104,** 381 (1987).
42. Chao, C. C., Duwez, P., and Tsuei, C. C., *J. Appl. Phys.* **42**(11), 4282 (1971).
43. Yuen, S., Chen, Y., Kubsh, J. E., Dumesic, J. A., and Topsøe, H., *J. Phys. Chem.* **86,** 3022 (1982).
44. Garten, R. L., Delgass, W. N., and Boudart, M., *J. Catal.* **18,** 90 (1970).
45. Balse, V. R., Sachtler, W. M. H., and Dumesic, J. A., *Catal. Lett.* **1,** 275 (1988).
46. Feeley, J. S., and Sachtler, W. M. H., *Zeolites* **10,** 738 (1990).
47. Mydosh, J. A., and Nieuwenhuys, G. J., *in* "Ferromagnetic Materials I" (E. P. Wohlfarth, Ed.), p. 73. North Holland Pub., Amsterdam, 1988.
48. van't Bilk, H. F. J., van Zon, J. B. A. D., Huizinga, T., Vis, J. C., Koningsberger, D. C., and Prins, R., *J. Am. Chem. Soc.* **107,** 3139, 3139 (1985).
49. Wielers, A. F. H., Kock, A. J. H. M., Hop, C. E. C. A., Geus, J. W., and van der Kraan, A. M., *J. Catal.* **117,** 1 (1989).